

PHASE TRANSITIONS

Nondeterministic dynamics in the η -to- θ phase transition of alumina nanoparticles

Masaya Sakakibara¹, Minoru Hanaya², Takayuki Nakamuro^{1*}, Eiichi Nakamura^{1*}

Phase diagrams and crystallography are standard tools for studying structural phase transitions, whereas acquiring kinetic information at the atomistic level has been considered essential but challenging. The η -to- θ phase transition of alumina is unidirectional in bulk and retains the crystal lattice orientation. We report a rare example of a statistical kinetics study showing that for nanoparticles on a bulk Al(OH)_3 surface, this phase transition occurs nondeterministically through an ergodic equilibrium through the molten state, and the memory of the lattice orientation is lost in this process. The rate of the interconversion was found to be insensitive to the electron dose rate, and this process had a small Gibbs free energy of activation. These nondeterministic kinetics should be a key feature of crystal nucleation occurring in high-surface-energy regions of bulk crystals.

Crystal phase transitions are often irreversible and thus deterministic processes. For example, alumina (Al_2O_3) undergoes a series of irreversible first-order phase transitions with increasing temperature as it transforms from hydrated alumina [bayerite, $\alpha\text{-Al(OH)}_3$] into the metastable η phase, the θ phase, and finally the most stable α phase previously reported (Fig. 1A) (1). The transitions involve a series of Al–O bond cleavages that increase in the aluminum atom coordination, from a 3:5 ratio of 4- and 6-coordinate in the η phase, an equal mix in the θ phase, to all 6-coordinate in the α -phase. Previous bulk crystallographic studies concluded that the orientation of the anion sublattice is retained during the η -to- θ transition, although the reasons for this were not fully understood (2, 3).

To investigate this transformation further, we focused on surface regions where nucleation initiates the bulk phase transition. We studied nanosized particles (NPs) of alumina that formed on a bulk surface of $\alpha\text{-Al(OH)}_3$ crystallites prepared at submicrometer scale on a spherical aggregate of an amminated carbon nanotube ($a\text{CNT}$) (Fig. 1B). The reactions were then monitored *in situ* with angstrom- and millisecond-resolution transmission electron microscopy (TEM) at 80 kV. At temperatures between 110 and 298 K, $\alpha\text{-Al(OH)}_3$ dehydrated (2) to form an alumina melt. From this melt, a mixture of NPs formed that underwent various equilibria transitions (η -to- θ , θ -to- η , η -to- η , and θ -to- θ) through a molten state (ML) of alumina (Fig. 1C, 20.02 s and 35.60 s) under the influence of a high surface energy. The surface energy of alumina NPs with diameters smaller than ~4 nm makes ML as stable as crystalline states (4), as opposed to the bulk thermodynamics, where

ML becomes the most stable only at 2300 K. Here, the η -to- η and θ -to- θ transitions refer to the NP changing its orientation relative to the bulk Al(OH)_3 substrate.

Thus, the η -to- θ phase transition of alumina, which is unidirectional in bulk, occurs nondeterministically through a rapid η/θ equilibrium that occurs through melting and recrystallization of NPs on the bulk Al(OH)_3 surface (Fig. 1, D and E). Also, we found that the memory of the lattice orientation was lost. For single NPs, the ratio of time spent in the η and θ forms converged after ~1 min at 298 K. This ratio matched the number of η and θ NPs formed when the equilibrium stopped as the NPs grew larger and the surface energy decreased. These observations conform to the ergodicity concept in statistical mechanics; that is, the system explores all parts of its available phase space versus becoming kinetically trapped (5–7).

The phase transition was driven thermally because of underlying high surface energy, as evidenced by the data showing that the phase transition rate, expressed as the observation time in seconds [k (s⁻¹)], depended on the temperature of the sample stage but not the electron dose rate (EDR). The TEM observations indicated that the recrystallization step was rate limiting and occurred >100 times more slowly than the melting step, which took place in <3 ms at 298 K (8). Statistical kinetic analysis on individual NPs at 110 and 298 K provided a set of kinetic parameters of the η/θ interconversion, an Arrhenius frequency factor ($A = 20.9 \text{ s}^{-1}$), an Arrhenius activation energy ($E_a = 2.62 \text{ kJ mol}^{-1}$), a large negative activation entropy ($\Delta S^\ddagger = -230 \text{ J mol}^{-1} \text{ K}^{-1}$), and a Gibbs free energy of activation ($\Delta G^\ddagger = 68.0 \text{ kJ mol}^{-1}$), indicating that the sluggishness of the recrystallization arises from entropic penalty (9, 10). Not unexpectedly, the magnitude of the ΔG^\ddagger value was comparable to those of common organic chemical reactions taking place at room temperature. These data

represent a rare demonstration of the capability of real-space TEM observation for elucidation of the mechanism of chemical events through statistical mechanical analysis (11, 12).

These kinetics data obtained for NPs grown from Al(OH)_3 crystallites align with the thermodynamics of nanosized alumina polymorphs that Navrotsky *et al.* studied for NPs prepared by gas-phase condensation (13). The Navrotsky data, combined with the data that we present here, suggest that nondeterministic kinetics is a common feature of crystal nucleation in high-surface-energy regions of alumina crystals. The discrepancy between the lattice retention in bulk and the scrambling at the nanoscale suggests that the bulk experiment observations (4) result from an interplay between localized disorder in high-energy nanoregions and the overarching order imposed by the surrounding bulk crystal structure (14). Combined with the atomistic mechanism of bulk crystal disordering (15), this disparity challenges traditional views of phase transitions based on macroscopic analyses and underscores the necessity for caution when extrapolating macroscopic data to comprehend their atomistic mechanism. The observed kinetics and the EDR insensitivity indicate that the surface energy is more influential than has been generally assumed in the atomistic event on bulk surfaces and defects or in nanoscale materials that are often studied by high-resolution TEM (16).

Alumina nanoparticle formation on Al(OH)_3

We used single-molecule atomic-resolution time-resolved electron microscopy (SMART-EM) (17–20) to cinematographically analyze individual chemical events on single molecules or nanometer-sized specimens supported on CNTs in vacuum (21). The method provides the highest spatio-temporal resolution available for the given instrumentation, operating under high-vacuum and variable temperature and voltage conditions with a useful frame rate of 1000 frames per second (fps) (15, 22, 23). This capability was essential to study the faint contrast of aligned oxygen atoms in alumina NPs (24). In this context, we have developed a method to grow alumina NPs on the surface of $\alpha\text{-Al(OH)}_3$ (Fig. 1C). By mixing a water-dispersible spherical aggregate of $a\text{CNT}$ with an aqueous solution of NaAlO_2 (25) and allowing the mixture to stand at room temperature, we formed a thin crust of polycrystals of $\alpha\text{-Al(OH)}_3$ on the ~100-nm-sized $a\text{CNT}$ aggregate. Neither pristine CNT nor oxidized CNT produced 100-nm-sized solid crystals instead of a crust of $\alpha\text{-Al(OH)}_3$ crystallites (fig. S3).

The average size of the $\alpha\text{-Al(OH)}_3$ crystallites was 4.7 nm, as estimated by powder x-ray diffraction (fig. S2). The shell of the $\alpha\text{-Al(OH)}_3$ polycrystals served as the seed for the alumina crystallization (compare with Fig. 1C). Thermo-gravimetric and differential thermal analysis

¹Department of Chemistry, The University of Tokyo, Bunkyo-ku, Tokyo, Japan. ²Graduate School of Science and Technology, Gunma University, Kiryu, Gunma, Japan.

*Corresponding author. Email: muro@chem.s.u-tokyo.ac.jp (T.N.); nakamura@chem.s.u-tokyo.ac.jp (E.N.)

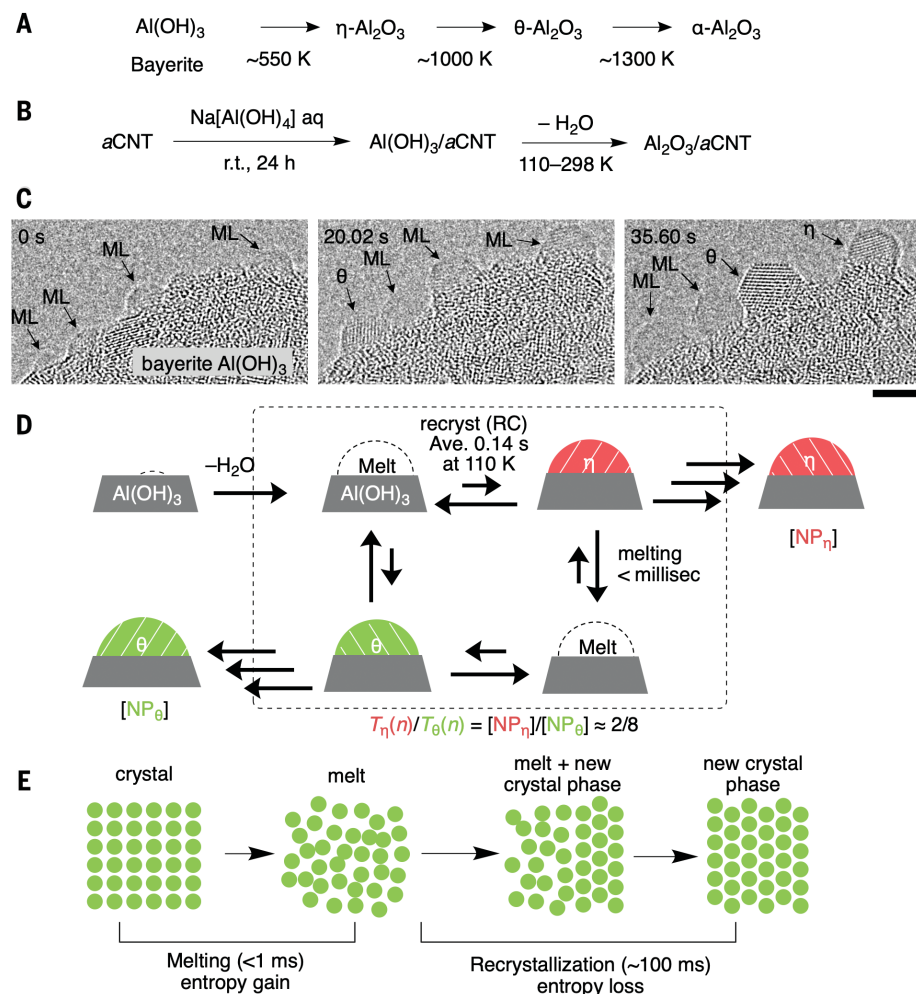


Fig. 1. Conversion of $\alpha\text{-Al(OH)}_3$ to η and θ alumina. (A) The macroscale thermal transformation of $\alpha\text{-Al(OH)}_3$ to $\alpha\text{-Al}_2\text{O}_3$ is an irreversible phase transition. (B) Preparation of $\alpha\text{-Al(OH)}_3$ on a spherical aggregate of aCNT (see text). (C) Representative TEM images (50 fps) of in situ formation of alumina NPs. The aggregates of ~100-nm-diameter $\alpha\text{-Al(OH)}_3$ nanocrystallites formed on the surface of a spherical aggregate of aCNT. ML represents a molten state consisting of a mixture of melt and growing crystal, where we found few discernable lattices in the 50-fps images, and η and θ represent NP $_\eta$ and NP $_\theta$, respectively. The gray area at the top is a vacuum. See the supplementary materials for a low-magnification image of the Al(OH)₃/aCNT crystallites on the spherical aggregate of aCNT (fig. S1). Scale bar, 3 nm. (D) Summary of the ergodic equilibria of alumina NPs through melting and recrystallization of the melt that resulted in the loss of memory of lattice orientation (stripes). $T_\eta(n)/T_\theta(n)$ is defined as the ratio of time each NP spent in the NP $_\eta$ -to-NP $_\theta$ state. [NP $_\eta$] and [NP $_\theta$] indicate the structural information after nucleation. (E) Schematic diagram of the observed mechanism of transformation mediated by the molten phase.

of the Al(OH)₃/aCNT samples showed a transformation sequence from $\alpha\text{-Al(OH)}_3$ to $\eta\text{-Al}_2\text{O}_3$ at 520 K, then to $\theta\text{-Al}_2\text{O}_3$ around 1000 K, and finally to $\alpha\text{-Al}_2\text{O}_3$ at ~1300 K, consistent with transitions reported for bulk $\alpha\text{-Al(OH)}_3$ (Fig. 1A and fig. S2) (3). The nanosized $\alpha\text{-Al(OH)}_3$ crystallites dehydrated into a mixture of $\eta\text{-Al}_2\text{O}_3$ and $\theta\text{-Al}_2\text{O}_3$ under the high-vacuum TEM observation (26), a process akin to the dehydrative production of α -alumina from nanosized boehmite [$\gamma\text{-Al(OH)}_3$] at room temperature upon ball milling (27). As discussed below, the electron beam-mediated dehydration occurred on the order of minutes,

whereas the thermal phase transitions of the NPs occurred in milliseconds (Fig. 2).

300-fps imaging of η / θ interconversion through melting and recrystallization

The transformation of an NP from the θ structure to the η structure at 298 K is shown as a series of images at 300 fps (3.33 ms per frame) in Fig. 2A. This transformation occurred in two steps, fast melting followed by rate-limiting crystal growth. We estimated that the θ structure disappeared in far less time than one frame, but likely in under 1 ms, because we observed

only the η structure in the 30.0- to 33.3-ms frame and only the θ structure in the 33.3- to 36.7-ms frame. After the rapid melting in the 33.3-ms frame, we observed the slow formation of the η crystal from the melt (28). The recrystallization process required ~100 ms to complete, which is >100 times longer than the melting process. Note that the rate-limiting step of such a multi-step reaction was identified visually rather than being determined by kinetic analysis.

In the 30.0-ms frame, we saw the θ phase on the top right part (Fig. 2A, green), which, in the 33.3-ms frame, has disappeared to produce a melt, and the η phase on the bottom left (Fig. 2A, red). The η -crystalline phase continued to expand toward the top right region, where we had seen the θ structure several milliseconds earlier. Using two-dimensional (2D) fast Fourier transform (FFT) analyses, we determined the orientation of the anion sublattices. The 30.0-ms frame (Fig. 2B, green square) corresponds to the θ phase with a lattice spacing of 2.3 Å, while the 33.3-ms frame (Fig. 2B, red square) represents the η phase with a lattice spacing of 1.9 Å.

The θ -to- η transformation was quantified by the change in intensities of the 2D FFT peaks (Fig. 2C). Compared with the instantaneous θ -to- η melt transition, the melt-to- η transition was far slower, as evidenced by the increase of the red-colored area of η -structure plotted in Fig. 2D. Here, we observed in situ the nucleation and crystal growth process on the nanoscale, as illustrated in Fig. 1E (27, 29). The large difference in the rate constants between the crystal-to-melt and melt-to-crystal transitions suggested that the latter suffers an entropic penalty because it requires extensive atomic organization (13).

We analyzed the crystal lattice orientation before and after phase transitions and found that the orientation was randomized (Fig. 2, B and E), in contrast to the reported bulk observation (4). We measured the angles between the $\theta(310)$ and $\eta(400)$ planes during three-phase transition events and obtained varied values of 1.8° (Fig. 2B), 43.1° (Fig. 2E, left), and 77.6° (Fig. 2E, right). These findings were consistent with the formation of a molten state in which substantial atomic relocations and extensive alternation of Al–O bonds took place (compare with Fig. 1E). Thus, the phase change at the nanoscale occurred through a reconstructive mechanism instead of by direct transformation from one crystal plane to a specific other plane, as occurs in martensitic transformation or cation diffusion within the anion sublattice (30). In good agreement with the reconstructive mechanism, we determined a highly negative entropy of activation of the recrystallization step (discussed below).

Interconversions of η and θ alumina at 110 K

We next performed statistical analysis to determine the energetics of the dynamics at 110 K.

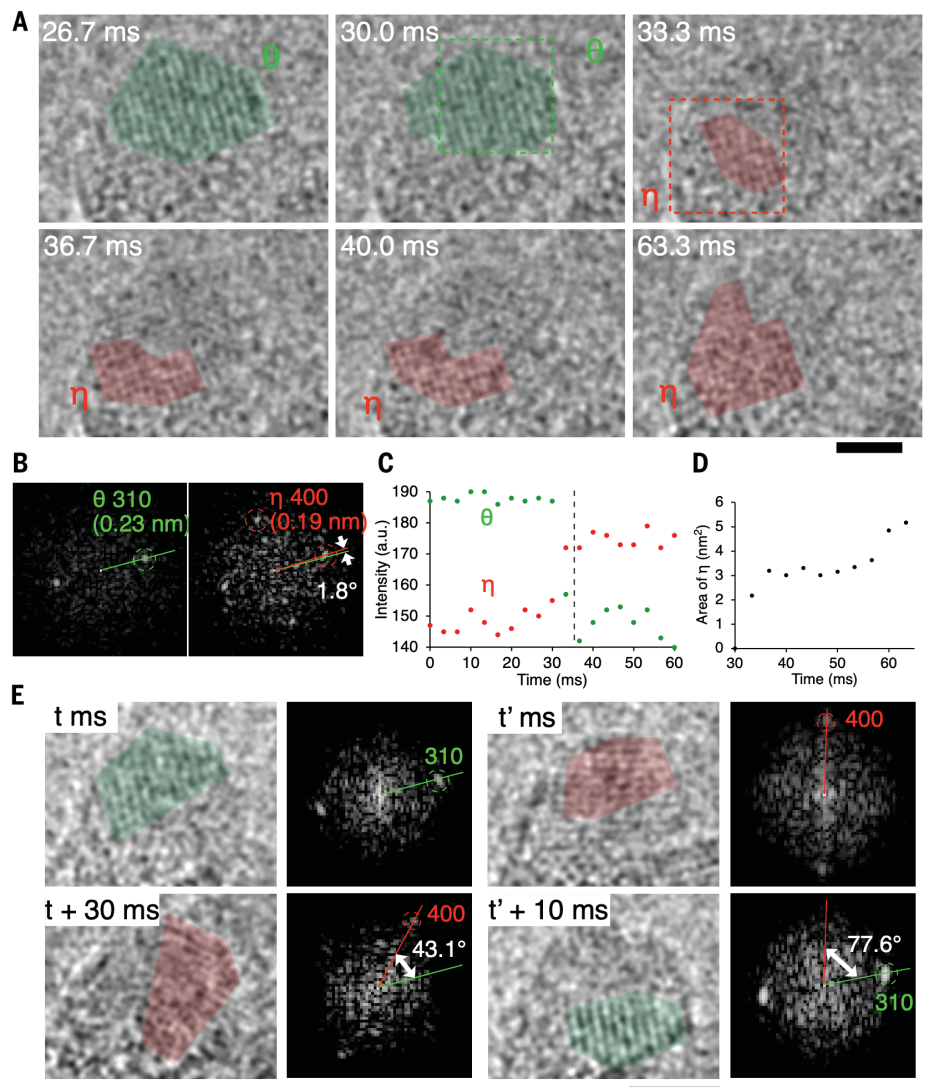


Fig. 2. Observation of phase transition by 300-fps imaging at 298 K. (A and B) Representative TEM images of a nucleating NP and their 2D FFT patterns (fig. S4 and movie S1). EDR = $2.2 \times 10^6 \text{ e}^- \text{ nm}^{-2} \text{ s}^{-1}$, 80 kV, with the K3-IS camera. Scale bar, 2 nm. Local structures were classified into θ (green) and η (red) based on 2D FFT analysis. (C) Time evolution of the intensity of the strongest peaks in 2D FFT pattern for the θ (green) and η (red) phases. (D) Time course of the increase of the projected area of η crystal for the TEM image [e.g., the red area in (A)]. (E) Measurement of the angle between the $\theta(310)$ and $\eta(400)$ planes before and after the transformation. For TEM images with 2D lattice fringes, the structure was assigned by comparing with simulated images in terms of both lattice spacing and symmetry. For TEM images with only a 1D lattice fringe, the frames with a 0.19-nm spacing [$\eta(400)$] are classified as η , and those with a 0.23-nm spacing [$\theta(310)$] are classified as θ .

We studied tens of NPs cinematographically at 110 K and 50 fps. Figure 3A illustrates an example observation of a single NP for 100 s (see also Fig. 1C). Small bulges on the $\text{Al(OH)}_3/\text{acNT}$ surface appeared first (31). Initially, up to a projected area of $\sim 3 \text{ nm}^2$ (0 s), we saw no structural features. As the size of these bulges increased, the structure of the single NP fluctuated stochastically between η structures (22.46, 79.72, and 99.80 s) and θ structures (20.44 and 47.88 s) transforming through the ML (54.36 s and 56.76 s). The ML, which is

a mixture of the melt and a growing crystal, produced no discernable lattice image in the 50-fps images.

We assigned the structure by 2D FFT analysis (fig. S6). During the course of 10 to 20 s, the NP frequently switched between η (Fig. 3B, red) and θ (Fig. 3B, green). The changes for 12.0 to 13.0 s and for 15.6 to 16.6 s indicated that the interconversions were stochastic at any given point (32, 33). The observation of the ML (black) over several consecutive frames was the result of slow crystal growth, as discussed above. Although

the lifetime of each state changed stochastically (26, 34, 35), an average over a sufficiently long time revealed that the ratio of the time the NP spent in NP_η to NP_θ (T_η/T_θ) reached a constant value, as discussed below.

As the electron beam-mediated Al(OH)_3 -to-alumina conversion proceeded, the NP grew larger and its projected area increased from 2 to 8.5 nm^2 after 100 s (Fig. 3C, black dots), which was thousands of times slower than the thermal melting and recrystallization process (Fig. 2A). For the NP of projected area 3 to 6 nm^2 , the two phases interconverted frequently with a frequency of 1.19 Hz, corresponding to a reaction rate constant $k = 1.19 \text{ s}^{-1}$, or one event every 840 ms on average. This frequency gradually decreased, and the interconversion stopped when the reduced contribution of surface energy, observed as the projected area of the NPs, reached an average size of 7.88 nm^2 (Fig. 3D).

Figure 3E illustrates the “convergence of time averages,” a basic aspect of statistical mechanical analysis. The T_η/T_θ ratio varied and the proportion of η changed appreciably from 0.05 to 0.45 in short observations (1 to 5 s) but converged to a constant value after 20 s. The convergence time constant (τ) was 9.0 s, indicating the time required for the deviation from the long-term average to reduce to e^{-1} . Therefore, time scales longer than $\tau = 9.0 \text{ s}$ reflected statistically meaningful properties of the system. Figure 3F shows the frequency of alternation between the η and θ phases during 10-s intervals between 0 and 100 s. As the projected area of the NP slowly increased (black dots), the converged T_η/T_θ ratio averaged 0.17/0.83 between 10 and 70 s.

Figure 3G shows a finer-resolution series at $\sim 82.72 \text{ s}$ (purple line), when the projected area was 7.52 nm^2 and the η/θ interconversions ceased and stabilized as NP_η ($T_\eta/T_\theta = 1/0$). This change indicated that the interconversion was quenched by a decrease in the surface energy. Figure 3H summarizes the duration of the ML (Fig. 3B, black bar) at 110 K, representing the time required for recrystallization: the average time of 0.14 s and the maximum time of 0.96 s. The final state of the 10 NPs that we studied in detail showed a ratio of $[\text{NP}_\eta]/[\text{NP}_\theta] = 2/8$ (fig. S7). This value agreed with the $T_\eta/T_\theta = 0.17/0.83$ discussed above. This observation of “equivalence of time and ensemble averages” evidenced the ergodicity of the η/θ interconversions.

Interconversions of η and θ alumina at 298 K

Statistical analysis of the behavior of individual alumina NPs at 110 K showed that the η/θ equilibrium follows the ergodic principle of statistical mechanics. This indicates that studying a single NP or several NPs over a sufficiently long time provides statistically meaningful insights into the reaction mechanism. Therefore,

we repeated the same set of experiments at 298 K and determined the kinetic and thermodynamic parameters of the η/θ equilibrium process.

Like the observations at 110 K, we saw reversible interconversions (Fig. 4A) between η (such as at 5.06 s), θ (such as at 27.72 s), and ML (such as at 37.62 s) at 298 K. Data from one of the 13 NPs examined are shown in Fig. 4, A to E. Over a period of 60 s, the projected area of the NP grew from 2 to 16 nm², and interconversions between the η and θ phases were observed over the 3- to 12.5-nm² range. The shape of the NP gradually changed with the η/θ structural transition. Analyzing changes between 33.84 and 33.88 s (Fig. 4B), we found that the orientation of the crystals shifted and the NP surface moved at a minimum rate of ~ 0.01 nm/ms. This shape flexibility was consistent with the melting and crystal growth mechanism and lattice scrambling in Fig. 2E. [We note in passing that higher-temperature (473 K) analysis was not possible because Al(OH)₃ was converted entirely to alumina before analysis, and atomic resolution imaging at a midtemperature (200 K) analysis was unfeasible because of instability of the view field caused by evaporation of liquid nitrogen (fig. S8).]

With EDR = 3.2×10^6 e⁻ nm⁻² s⁻¹ at 80 kV, the projected area increased from 2 to 16 nm² (Fig. 4C, black dots). The rate constant of the η/θ interconverting was $k = 7.27$ s⁻¹, or one event every 138 ms on average, measured over the 3- to 6-nm² range; this was 6.1 times more frequent than at 110 K. We also observed a “convergence of average” at 298 K, and the convergence time constant of $\tau = 1.6$ s was 5.6 times shorter compared with that at 110 K (Fig. 4D). The converged T_η/T_θ ratio was 0.20/0.80 (Fig. 4E), which was slightly greater than that of 0.17/0.83 at 110 K.

The interconversion rate k was insensitive to the EDR for a NP of the same size (5 nm²). As shown in Fig. 5A, the ERD variation at 298 K between 3.2 and 6.4×10^6 e⁻ nm⁻² s⁻¹ did not affect the rate constant of the interconversion to be $k = 7.42 \pm 0.08$ (SE) s⁻¹, nor did the $T_\eta/(T_\eta + T_\theta)$ ratio, where k does change upon the temperature variation of the sample stage. This result indicated that the electron beam had negligible effects on the rate of the η/θ transition in the alumina NPs on bulk Al(OH)₃, where the high surface energy of the NP and the thermal energy from the stage drove the reaction. This result is also consistent with the observation that the rate-limiting step is the entropy-controlled recrystallization instead of the melting (Fig. 1E).

At 298 K, the increased thermal energy imparted to the particles allowed the interconversion between η and θ to continue beyond the projected area of 8 nm². However, as the NP size increased, the interconversion frequency

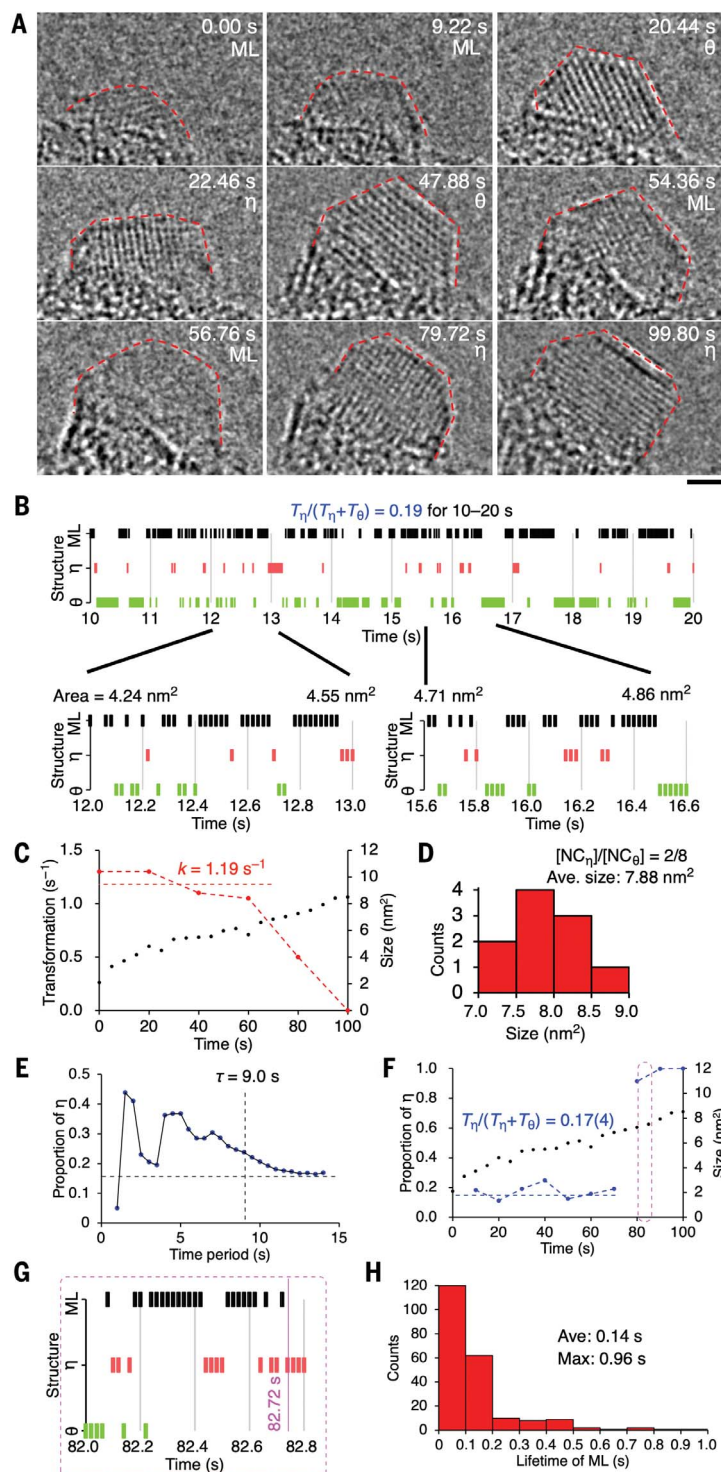
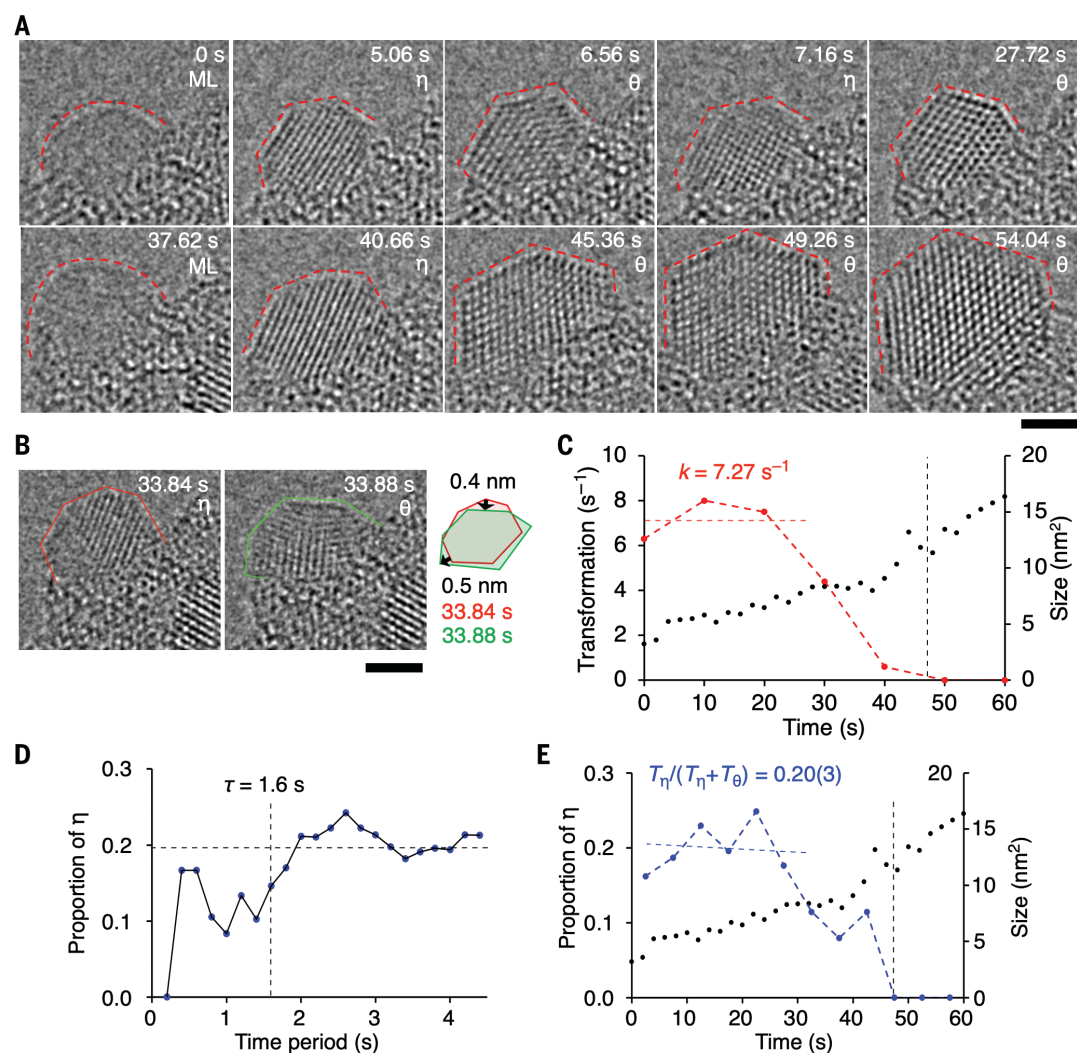


Fig. 3. Structural fluctuations of alumina NPs at 110 K. (A) Representative TEM images of an alumina NP at 50 fps. EDR = 2.9×10^6 e⁻ nm⁻² s⁻¹. Scale bar, 1 nm. The gray top area is a vacuum, and the bottom is the α -Al(OH)₃ crystallite (fig. S5 and movie S2). (B) Time evolution of the structure of the NP during 10 to 20 s and its close-up versions. (C) Time-course analysis of the η/θ interconversion frequency (red) with the size of the NP (black). (D) Statistical analysis of the critical size of alumina for structural freezing. (E) Convergence of the η/θ ratio with extended averaging time. (F) Time-course analysis of the proportion of η structure (blue) during 10-s intervals between 0 and 100 s. (G) Close-up plot of the structure of the NP around 82.44 s. (H) Statistics of the lifetime of ML at 110 K.

Fig. 4. Formation and structural fluctuation of alumina NPs at 298 K. (A) Representative TEM images of an alumina NP. At 50 fps, EDR = $3.2 \times 10^6 \text{ e}^- \text{ nm}^{-2} \text{ s}^{-1}$, 80 kV. Scale bar, 1 nm (fig. S8 and movie S3). (B) Shape changes of the cluster during the interconversion. (C) Time-course analysis of the η/θ interconversion frequency (red) with the size of the NP (black). (D) Convergence of the η/θ ratio with extended averaging time at the diameter of ~3 nm. (E) Time-course analysis of the proportion of η structure (blue) with the averaging period of 5 s.



gradually dropped (Fig. 4C), and the interconversion completely stopped once the size reached 12.5 nm^2 . This freezing size corresponded to $\sim 150 \text{ Al}_2\text{O}_3 units, ~ 1.5 times larger in volume than the $\sim 100 \text{ Al}_2\text{O}_3 units at 110 K. Note that the NP is seen here as a macromolecule made of 150 Al_2O_3 units. As the size increased, the T_η/T_θ ratio dropped to $<1/9$, eventually forming NPs composed entirely of the θ phase (Fig. 4A, 54.04 s). When the structures froze, all 13 NPs we studied were in the θ form (fig. S10), demonstrating the equivalence of time and ensemble averages at 298 K.$$

Discussion

In terms of crystal nucleation, the most important finding of this study was the stochastic appearance of the η and θ structures preceding the formation of a stable crystalline phase in the NP experiments. These events were driven by the surface and thermal energy, as evidenced by their insensitivity to EDR, much slower kinetics compared with electron beam-driven Al(OH)_3 dehydration, and the kinetic parameters discussed below. We suspect that this

dominance of surface and thermal energy may be common for the nanoscale TEM observations, because we recently observed a similar occurrence in the nucleation of CsCl nanocrystals (36). To investigate this further, we conducted a quantitative statistical analysis of the ergodic equilibria under the 110 and 298 K conditions, studying single NPs for a period longer than the convergence time (τ). We estimated the energetics of η/θ interconversion in NPs of $\sim 20 \text{ nm}^3$ using the temperature dependency of the T_η/T_θ ratio and the rate constant (k) obtained statistically for single NPs at 110 and 298 K (37). The increase of the T_η/T_θ ratio from 0.17/0.83 at 110 K to 0.20/0.80 at 298 K indicates that NP_η is thermodynamically less stable than NP_θ by $\Delta H = 0.29 \text{ kJ/mol}$. The differences in entropy and free energy associated with the η -to- θ interconversion were calculated from the equilibrium constant (Fig. 5C; for details, see figs. S11 and S12).

The η/θ interconversion rate, which reflects the energetics of the rate-limiting recrystallization step, increased from $k = 1.19 \text{ s}^{-1}$ at 110 K to $k = 7.27 \text{ s}^{-1}$ at 298 K, indicating an Arrhenius

frequency factor of $A = 20.9 \text{ s}^{-1}$ and an activation energy (E_a) of 2.62 kJ mol^{-1} (Fig. 5B). We calculated $\Delta H^\ddagger = 0.14 \text{ kJ mol}^{-1}$ using the equation $E_a = \Delta H^\ddagger + RT$, where $RT = 2.48 \text{ kJ mol}^{-1}$ is the thermal energy at 298 K. From ΔH^\ddagger and the Eyring equation, we calculated an entropy of activation, $\Delta S^\ddagger = -230 \text{ J mol}^{-1} \text{ K}^{-1}$, an extremely large entropy loss due to recrystallization of the molten phase into η or θ phase. Using this dataset, we estimated the activation free energy of the η/θ interconversion to be $\Delta G^\ddagger = 68.0 \text{ kJ mol}^{-1}$, which in turn reproduces the observed rate constant k at 298 K (fig. S11 and Eqs. 1 to 6 in the supplementary materials). The recrystallization step suffered from an entropy decrease, whereas the melting step benefited from an entropy increase (compare with Fig. 2). Thus, the η -to- θ interconversion is a rare example of reactions that are controlled solely by the entropy barrier with virtually no enthalpy barrier.

The extremely small activation enthalpy ($\Delta H^\ddagger = 0.14 \text{ kJ mol}^{-1}$) of the η/θ equilibrium through the ML state suggests that the ML state and the η and θ crystalline state of the alumina

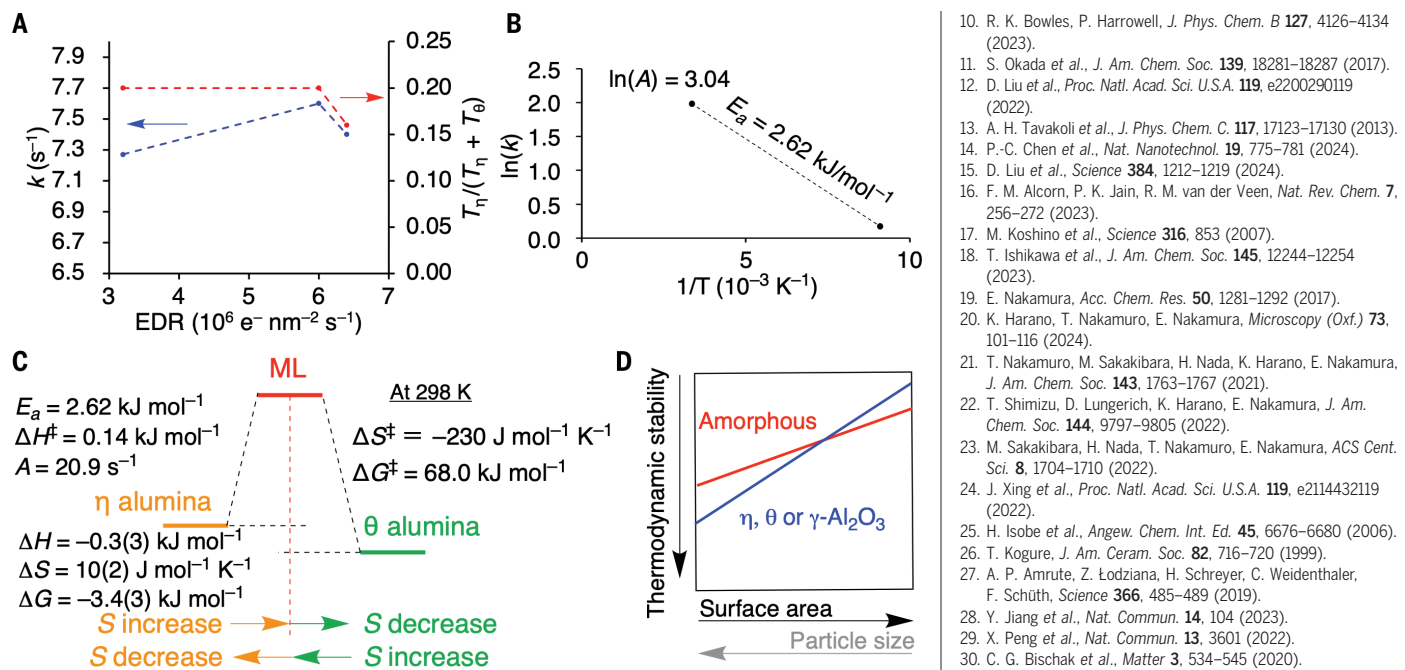


Fig. 5. Kinetics and thermodynamic analysis. (A) Insensitivity of k and the $T_n/(T_n + T_\theta)$ ratio to EDR at 298 K. (B) Arrhenius plot of the temperature dependence of k . (C) Energy diagram on statistical kinetics of individual NPs of $\sim 20 \text{ nm}^3$ in volume. The energetic parameters are shown per mole of NPs. (D) Navrotsky's surface energy/stability diagram on alumina polymorphs (arbitrary scale). The crossing point reported for γ -alumina NPs corresponds to a volume of $\sim 50 \text{ nm}^3$ (17). The crossing point determined in this study for the η - and θ -alumina NPs is $\sim 20 \text{ nm}^3$.

NPs of $\sim 20 \text{ nm}^3$ in volume have nearly the same enthalpy (Fig. 5C). This conclusion aligns with Navrotsky's thermodynamic data showing that the enthalpy difference becomes zero for amorphous alumina NPs and γ -alumina NPs at a volume of $\sim 50 \text{ nm}^3$ (Fig. 5D) (1, 4). The discrepancy in the volume between 20 and 50 nm^3 may have been caused by the presence of an $\text{Al}_2\text{O}_3/\text{Al(OH)}_3$ interface in the present study. In cases where E_a approaches zero, the accuracy of the derived activation parameters may become uncertain and reflect inherent limitations of the Arrhenius model, which assumes a clear exponential dependence of the rate constant on temperature.

The SMART-EM study of the alumina NP system provided a unique opportunity to perform a statistical mechanical analysis of the chemical kinetics. The observed crystal melting and recrystallization using real-space TEM imaging parallels our recent reciprocal space study on crystal melting (20). Through this comparison, we found that the electron beam drives the bulk disordering studied under electron diffraction (ED) conditions, whereas the nanoscale phase transition discussed herein is driven thermally because of the underlying high surface energy (38). Therefore, the former has a rate constant and Arrhenius frequency

factor (A) with units of $(\text{e}^{-})^{-1} \text{ nm}^2$, whereas the latter has units of s^{-1} . This difference, along with the temperature dependence of the reaction rate, as described by the Arrhenius equation, $k = A \exp(-E_a/RT)$, makes comparing the reaction rates between the two systems complex. Furthermore, our recent statistical mechanical kinetic studies of electron beam-driven reactions have revealed temperature- and voltage-dependent switching among multiple mechanisms (15, 16). Our data underscore the importance of careful kinetic and thermodynamic studies to accurately infer mechanisms for the atomistic phenomena observed under TEM and ED conditions.

REFERENCES AND NOTES

- I. Levin, D. Brandon, *J. Am. Ceram. Soc.* **81**, 1995–2012 (1998).
- R.-S. Zhou, R. L. Snyder, *Acta Crystallogr. B* **47**, 617–630 (1991).
- S. Ishizuka et al., *Chem. Mater.* **28**, 8732–8741 (2016).
- J. M. McHale, A. Auroux, A. J. Perrotta, A. Navrotsky, *Science* **277**, 788–791 (1997).
- D. J. Smith, A. K. Petford-Long, L. R. Wallenberg, J.-O. Bovin, *Science* **233**, 872–875 (1986).
- S. Iijima, T. Ichihashi, *Phys. Rev. Lett.* **56**, 616–619 (1986).
- J.-Y. Li et al., *Proc. Natl. Acad. Sci. U.S.A.* **121**, e2314797121 (2024).
- B. J. Siwick, J. R. Dwyer, R. E. Jordan, R. J. D. Miller, *Science* **302**, 1382–1385 (2003).
- D. Frenkel, *Physica A* **263**, 26–38 (1999).
- R. K. Bowles, P. Harowell, *J. Phys. Chem. B* **127**, 4126–4134 (2023).
- S. Okada et al., *J. Am. Chem. Soc.* **139**, 18281–18287 (2017).
- D. Liu et al., *Proc. Natl. Acad. Sci. U.S.A.* **119**, e220290119 (2022).
- A. H. Tavakoli et al., *J. Phys. Chem. C* **117**, 17123–17130 (2013).
- P.-C. Chen et al., *Nat. Nanotechnol.* **19**, 775–781 (2024).
- D. Liu et al., *Science* **384**, 1212–1219 (2024).
- F. M. Alcorn, P. K. Jain, R. M. van der Veen, *Nat. Rev. Chem.* **7**, 256–272 (2023).
- M. Koshino et al., *Science* **316**, 853 (2007).
- T. Ishikawa et al., *J. Am. Chem. Soc.* **145**, 12244–12254 (2023).
- E. Nakamura, *Acc. Chem. Res.* **50**, 1281–1292 (2017).
- K. Harano, T. Nakamuro, E. Nakamura, *Microscopy (Oxf.)* **73**, 101–116 (2024).
- T. Nakamuro, M. Sakakibara, H. Nada, K. Harano, E. Nakamura, *J. Am. Chem. Soc.* **143**, 1763–1767 (2021).
- T. Shimizu, D. Lungerich, K. Harano, E. Nakamura, *J. Am. Chem. Soc.* **144**, 9797–9805 (2022).
- M. Sakakibara, H. Nada, T. Nakamuro, E. Nakamura, *ACS Cent. Sci.* **8**, 1704–1710 (2022).
- J. Xing et al., *Proc. Natl. Acad. Sci. U.S.A.* **119**, e2114432119 (2022).
- H. Isobe et al., *Angew. Chem. Int. Ed.* **45**, 6676–6680 (2006).
- T. Kogure, *J. Am. Ceram. Soc.* **82**, 716–720 (1999).
- A. P. Amrute, Z. Łodzińska, H. Schreyer, C. Weidenthaler, F. Schüth, *Science* **366**, 485–489 (2019).
- Y. Jiang et al., *Nat. Commun.* **14**, 104 (2023).
- X. Peng et al., *Nat. Commun.* **13**, 3601 (2022).
- C. G. Bischak et al., *Mater. J.* **3**, 534–545 (2020).
- J. Li, Y. Li, Q. Li, Z. Wang, F. L. Deepak, *Nanoscale Horiz.* **4**, 1302–1309 (2019).
- S. Auer, D. Frenkel, *Nature* **409**, 1020–1023 (2001).
- Y. Kimura, H. Niinomi, K. Tsukamoto, J. M. García-Ruiz, *J. Am. Chem. Soc.* **136**, 1762–1765 (2014).
- J. Kotakoski, A. V. Krasheninnikov, U. Kaiser, J. C. Meyer, *Phys. Rev. Lett.* **106**, 105505 (2011).
- S. Jeon et al., *Science* **371**, 498–503 (2021).
- M. Sakakibara, T. Nakamuro, E. Nakamura, *ACS Nano* **18**, 22325–22333 (2024).
- S. S. Zumdhahl, S. A. Zumdhahl, D. J. DeCoste, *Chemistry* (Houghton Mifflin Harcourt, ed. 11, 2023), pp. 526–577.
- J. Sun et al., *Nat. Mater.* **13**, 1007–1012 (2014).

ACKNOWLEDGMENTS

We appreciate the thorough feedback provided by R. Clérac, M. Uwaha, D. Liu, and R. F. Egerton. M.S. thanks the Japan Society for the Promotion of Science (JSPS) and Forefront Physics and Mathematics Program to Drive Transformation (FoPM) for the fellowship. **Funding:** This work was supported by the Ministry of Education, Culture, Sports, Science and Technology (MEXT) (KAKENHI grant JP19H05459 to E.N.); JSPS (KAKENHI grants JP24H00447 to E.N. and JP23H04874 to T.N.); the JST PRESTO program (grant JPMJPR23Q6 to T.N.); and the Kazato Research Foundation (T.N.). **Author contributions:** Conceptualization: E.N., T.N.; Data acquisition: M.S.; Data analysis: M.S., T.N.; Funding acquisition: E.N., T.N.; Project administration: E.N., T.N.; Project supervision: E.N.; Writing—original draft: E.N., M.S., T.N.; Writing—review & editing: E.N., T.N., M.S., M.H. **Competing interests:** The authors declare no competing interests. **Data and materials availability:** All data necessary for evaluating the conclusions of this study are included in the main text or the supplementary materials. **License information:** Copyright © 2025 the authors, some rights reserved; exclusive licensee American Association for the Advancement of Science. No claim to original US government works. <https://www.science.org/about/science-licenses-journal-article-reuse>

SUPPLEMENTARY MATERIALS

- science.org/doi/10.1126/science.adr8891
- Materials and Methods
- Supplementary Text
- Figs. S1 to S12
- Movies S1 to S3
- References (39–48)

Submitted 24 July 2024; accepted 30 December 2024
10.1126/science.adr8891